Deep Learning-Oriented c-GAN Models for Vegetative Drought Prediction on Peninsular India

Jyoti S. Shukla ⓘ and Rahul Jashvantbhai Pandya ⓘ, *Senior Member, IEEE*

Abstract—In this article, the vegetative drought prediction employing Deep Learning (DL) models is designed, incorporating rainfall data and NOAA satellite-data-derived Vegetation Health Index (VHI) values spanning 1981–2022. Correspondingly, two DL-oriented models based on Generative Adversarial Networks (GANs): 1) Pix2Pix GAN (P2P) and 2) Bidirectional Convolutional LSTM (BiConvLSTM)-P2P GAN (BiCP2P) are developed over the targeted Region of Interest (ROIs). The assimilation of generative DL models for the application of drought forecasting constitutes a novel investigation and a state-of-the-art approach targeted in this work. Subsequently, the primary ROI designated is peninsular India, and the models. efficacy is validated by implementing it on two more ROIs: the Karnataka and Rajasthan states of India. The proposed models. outcomes are compared with several preferred methodologies quantitatively through Coefficient of Determination (R2 score), Mean Squared Error (MSE), and Mean Absolute Error (MAE) and qualitatively employing drought maps denoting the VHI-based drought severity levels over the ROI. Remarkably, excellent performance is demonstrated by the proposed models over peninsular India, with earned R2 score, MSE, and MAE values of 0.971, 0.0016, and 0.020 for P2P and 0.963, 0.0021, and 0.0239 for BiCP2P, respectively. Moreover, generated drought maps efficiently portrayed the drought severities across the land cover and could potentially be extended further for rapid drought risk assessments. The proposed models functioned outstandingly for the developed datasets on the ROIs, corroborating their potential for similar forecasting applications in other climatic zones, which can aid in better planning and preparedness to tackle natural predicaments such as drought calamity.

Index Terms—Deep learning (DL), drought prediction, peninsular India, Pix2Pix (P2P) generative adversarial networks GAN, vegetation health index (VHI).

I. INTRODUCTION

DROUGHT designates a prolonged absence of sufficient rainfall, resulting in catastrophic situations such as deteriorating gross agricultural developments and national economic growth [1]. As a consequence of deforestation, erratic rainfall, and escalating urbanization, droughts develop gradually and progressively; correspondingly, the type of drought ensuing is conditioned by various causative factors. However, the present article examines agricultural drought, tracking the green cover across the region of interest (ROI) over time and imbibing various state-of-the-art artificial intelligence (AI)/machine learning (ML) approaches. The availability of monumental satellite data and robust computational resources is presumptive for the research community's interest in analyzing and performing advanced remote sensing (RS) research which also serves as the foundation for the upsurge in deep learning (DL)-based methodologies for RS research. India relies intemperately on agriculture and annotates numerous states that experience drought annually, resulting in a detrimental impact on the national economy [2]. Furthermore, traditional drought prevention strategies appear partially effective owing to restricted knowledge about unanticipated geophysical consequences. Therefore, DL-based techniques embark on research opportunities, further exploring and extending the current solutions with data modeling for drought prediction.

A. Related Works

Recent research has substantially focused on aggregating RS data and AI/ML methodologies employing satellite or recorded meteorological data as input features to the models. Furthermore, in RS, the features commonly adopted are indices derived from satellite data, such as the vegetation condition index (VCI), temperature condition index (TCI), vegetation health index (VHI), normalized difference vegetation index (NDVI), soil adjusted vegetation index, enhanced vegetation index, and precipitation condition index. Similarly, indices produced from meteorological data, such as the standardized precipitation index, standardized precipitation evapotranspiration index, standardized streamflow index, and the rest, are frequently employed for drought modeling. In some research studies, meteorological and satellite data-derived indices are conflated, and subsequently, a comprehensive survey of drought prediction utilizing the indices is conducted [3], [4], [5], [6], [7], and [8]. Generally, it is customary to scrutinize the temporal change trends utilizing conventional statistical approaches in drought prediction as revealed in various studies involving models such as Sen's slope estimator, Mann-Kendall test, trend analysis employing linear regression (LR), and F-test, slope, and correlational statistics amid various parameters [4], [8], [9], [10], [11], [12], [13]. Moreover, the ML models for drought analysis and forecasting are pervasive, and several permutations have been implemented in the last decade. Correspondingly, a multitude of ML models, such as K-Nearest neighbor (KNN), random forest (RF), support vector

The authors are with the Electrical, Electronics, and Communications Engineering Department, Indian Institute of Technology, Dharwad 580011, India (e-mail: jyoti.shukla.21@iitdh.ac.in; rpandya@iitdh.ac.in).

machine (SVM), linear discriminant analysis, classification and regression tree, support vector regressor, radial basis function, LR, among others, have been rigorously compared to adjudge the most competent ML models [3], [13], [14], [15], [16]. Furthermore, a distinction is drawn among the types and sources of the indices proffered to the algorithms, i.e., between indices obtained from meteorological data and derived from satellite data and subsequently compared to demonstrate the efficacy of the drought indicators for various topologies [3], [4], [9], [13], [17].

Nevertheless, several DL algorithms have also proven effective on spatiotemporal (ST) datasets; models such as long short term memory (LSTM), convolutional neural networks (CNN), CNN-YOLO, multilayer perceptron, deep belief networks, autoregressive integrated moving average (ARIMA), hybrid wavelet networks, pretrained networks comprising ResNet and VGGnet, UNet, neural network models, and convolutional LSTM (ConvLSTM) models outperformed traditional models. Additionally, several research efforts exhibited the integrated permutations of the aforementioned DL models and illustrated their efficacy through comparative studies [4], [8], [17], [18], [19], [20], [21], [22], [23], [24]. On the other hand, ensemble techniques form a separate class of competitive models, where an ensemble is structured by merging different models' observations, outperforming other classical approaches by engrossing different models' rich features. Subsequently, ConvLSTM+SVM+RF, LR+RF, CNN+LSTM, and other model combinations have been asserted for use in such tasks [25], [26], [27]. Interestingly, numerous ingenious DL-oriented techniques have been applied recently for RS-based applications, among which a successful paradigm is originated by the consolidation of bidirectional ConvLSTM with the UNet (BiConvLSTM-UNet) [28], [29], [30]. Additionally, in the integrated BiConvLSTM-UNet model, for concatenating feature maps from the encoding and decoding routes, BiConvLSTM blocks are employed dissident to the ordinary skip connections of UNet encoder–decoder modules. Furthermore, in the current study, one of the other innovative DL models, generative adversarial networks (GANs), which belong to the generative class of DL models, is being probed for the application of drought monitoring and forecasting [31]. Notably, GAN has emerged as a cutting-edge model for a wide range of applications in recent years, with its extended versions becoming increasingly helpful in handling ST data for tasks such as the fusion of satellite datasets [32], ST prediction through integrated models [33], or change detection [34].

Successively, the conditional GAN (c-GAN) models pioneered the area of image-to-image translation by extending the traditional GAN model, as proposed by Mirza et al. [35]. Furthermore, Isola et al. [36] postulated Pix2Pix (P2P), a c-GAN-based architecture focusing on image-to-image translation and punctuated a generic approach, wherein the generation of an image is conditioned on a target image type. The P2P model comprises a generator and discriminator, where the generator transforms an input image from one domain into another, and the discriminator determines whether the given image is real or fake (generated). Besides, in the P2P model, the generator trains over an auxiliary $L2$ norm loss along with the standard adversarial loss. Remarkably, the P2P model is seldom implemented in the ST data processing, some of which encompass change detection of a specific land cover [37], [38] or harmonizing time series satellite data [39], among others. Nevertheless, the c-GAN model's potential for employing satellite-derived indices to predict droughts is yet to be thoroughly investigated to the author's best knowledge.

Consequently, two c-GAN approaches are suggested in this work for estimating vegetative drought: P2P and an integrated BiConvLSTM-P2P-GAN (BiCP2P). The models are applied to a temporal AVHRR sensor data amassed by the NOAA satellite series between 1981 and 2022, with peninsular India, Karnataka, and Rajasthan states of India selected as the ROIs. Subsequently, a quantitative analysis apropos the mean absolute error (MAE), mean squared error (MSE), and coefficient of determination (R2) score, along with a qualitative analysis through drought maps of the proposed models compared with the traditional ML/DL models is demonstrated.

B. Key Contributions

The major contributions of the current article are as follows.
1) A novel addition to drought prediction methodologies is the development of a drought forecasting and monitoring system established on the P2P-GAN model, which successfully maps the short-term land cover changes across the specified ROI based on historical RS data.
2) Second, a unique BiCP2P integrated model for drought estimation is designed, in which the P2P model is coupled with the BiConvLSTM module, which synthesizes the benefits of generative and temporal feature learning and may assist in vegetative dryness evaluation.
3) Third, to further instill diversity in the feature set equipped to the model training, the VHI and rainfall features are appended and stipulated concurrently in the dataset - IV, which represents a novel combination to the author's best knowledge for studying the influence of two prominent features in VHI-based drought prediction.
4) Furthermore, extensive investigation with the selection of ROI and datasets has been undertaken, aiming to validate the performance of the suggested models. Correspondingly, four datasets are developed: dataset - I represents the VHI dataset for peninsular India, which enunciates a significantly massive portion of India with various climatic fluctuations, dataset - II represents the VHI dataset for the subsetted region of the peninsula, the Karnataka state of India, an agriculturally dominant territory, dataset - III is upheld by the VHI values for a typically dry province of India with frequent drought episodes, the Rajasthan state, and dataset - IV constitutes a novel hybrid combination of meteorological data (rainfall characteristics) and satellite data features (VHI values).

The rest of this article is organized as follows. Section II details the datasets and preprocessing. Section III presents the methodology of the proposed models. Section IV encapsulates the results and discussions. Finally, Section V concludes this article.

II. Study Area, Datasets, and Preprocessing

The literature study reveals that meteorological data, such as precipitation and soil moisture, or a combination of satellite and meteorological data, are extensively employed for drought analysis. In the present work, the satellite data-derived VHI values and rainfall data as the meteorological counterpart are conceived for appointed ROIs to predict vegetative drought.

A. Study Area

India's peninsular region is the preferred research location for this study, which resembles a large inverted triangular area. Oceanic bodies surround the peninsula's three edges: the west with the Arabian Sea, the east with the Bay of Bengal, and the south with the Indian Ocean. The peninsula is the largest physiographic division of India, with a total area of around $1\,600\,000\,\text{km}^2$. Peninsular India's geography may be broadly categorized into the Deccan plateau, the central highlands, the Sahyadri mountain ranges sheltering the west, and the eastern ghats enveloping the east, encompassing vast stretches of states such as Maharashtra, Karnataka, and Tamil Nadu [40], [41]. As a result of dense, diverse geophysical features, the aforementioned topologies strongly influence climate shifts, sufficing to appoint peninsular India as ROI for dataset - I.

Successively, the peninsular dataset is narrowed to the state of Karnataka, which functions as an ROI for dataset - II and dataset - IV to determine the efficacy of the proposed DL models for a subset ROI with fewer characteristics. The ROI is situated in the Deccan plateau region, spanning $191\,791\,\text{km}^2$. Also, the Karnataka state's land cover is predominantly filled with agricultural and forest lands, making it an appealing ROI for vegetative drought prediction.

Additionally, to diversify the database further, the Rajasthan state of India is selected as the third ROI in this work, dedicated to the dataset - III. The Rajasthan state is one of India's most frequently drought-affected states; hence, it emerges imperative to examine the performance of the suggested models on such a topology. Furthermore, the ROI designates the largest province of India, encompassing $342\,239\,\text{km}^2$, with the state climate influenced by two main topological characteristics, the Aravalli Hills and the Thar desert located on the north-western periphery of the state.

The multispectral satellite images acquired through NOAA satellites' AVHRR sensors sheathed the globe. Moreover, the NOAA-derived VHI readings are sourced from STAR NESDIS's worldwide data, further filtered to the ROIs as exhibited in Fig. 1. With such assorted terrains dispersed over the ROIs, evaluating drought prevalence and vegetation health is arduous, albeit critical, to determine any potential socioeconomic distresses.

B. Satellite Data

Recently, the significant ascent in RS-based applications is attributed to the frequent revisiting rate and wide sweep width of satellites, rendering satellite data with greater ease [42]. Indices are markers applied to define the levels of a particular entity predicated upon several attributes, such as satellite data, that can further assist in estimating entities, notably land classes and
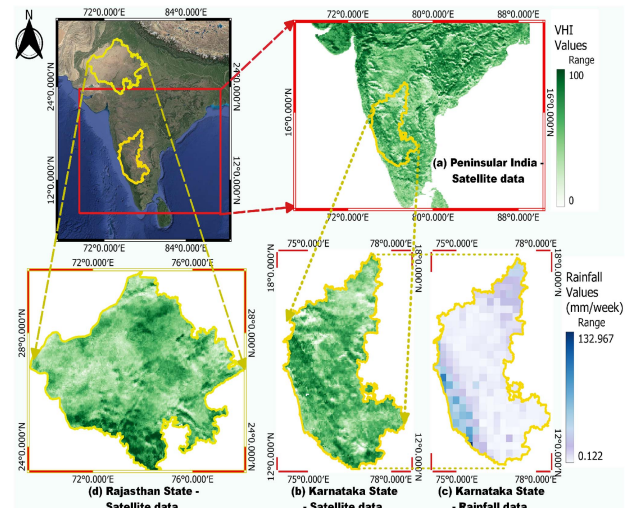

Fig. 1.   Study area and datasets. (a) Peninsular India satellite data, (b) Karnataka state satellite data, (c) Karnataka state rainfall data, and (d) Rajasthan state satellite data.

TABLE I
Vegetation-Based Indices

Indices	Formulae (i : pixel value)	Range
NDVI	$\dfrac{(NIR - RED)}{(NIR + RED)}$	[-1,1]
VCI	$\dfrac{NDVI_i - NDVI_{\min}}{NDVI_{\max} - NDVI_{\min}} * 100$	[0,100]
TCI	$\dfrac{BT_{\max} - BT_i}{BT_{\max} - BT_{\min}} * 100$	[0,100]
VHI	$a * VCI + (1 - a) * TCI$	[0,100]

vegetation cover, through reflectance readings from elements in different spectral bands. Subsequently, this work concentrates on the satellite data-derived vegetation-based indices, including NDVI, VCI, TCI, and VHI, delivering information on the green cover. Moreover, Table I exhibits the formulas used to compute the aforementioned indices, where NIR and RED represent the near-infrared (0.725–1.00 μm) and red (0.58–0.68 μm) spectral bands, respectively; BT denotes brightness temperature (in Kelvins), and $'a'$ dictates the contribution ratio between the VCI and TCI, which is adjusted to 0.5 for the present study.

Furthermore, VHI evaluates the vegetative healthiness of the ROI by factoring in the effects of temperature (TCI) and moisture (VCI). The VHI information generated by NOAA NESDIS STAR's Global and Regional Vegetation Health System (Center for Satellite Applications and Research) is adopted. The NOAA AVHRR sensors' weekly (7-day composite) globe data are contained within this database (https://www.star.nesdis.noaa.gov/smcd/emb/vci/VH/vh_ftp.php), possessing observations from the satellite series NOAA-6 through NOAA-19, which deliver data in six spectral bands. Subsequently, the weekly global VHI images were acquired from the 35th week of 1981 to the 25th week of 2022 for the current study, where the weekly VHI data are obtained by aggregating the daily AVHRR data for seven consecutive days imbibing a hybrid methodology. Moreover, the AVHRR dataset's NDVI and VCI values are smoothened (intended to pass through a data smoothening filter and gap-filling)

TABLE II
DROUGHT CATEGORY DEFINITION BY STAR NESDIS

Level	Description	VHI
-	Normal	> 40
D0	Abnormally dry	$36 - 40$
D1	Moderate drought	$26 - 35$
D2	Severe drought	$16 - 25$
D3	Extreme drought	$6 - 15$
D4	Exceptional drought	$0 - 5$

to compute the VHI [42]. Table II indicates drought severity levels categorized based on the VHI values upholding a direct proportionality with the vegetative health of the ROI [42].

1) Satellite Data Preprocessing: The VHI dataset is cropped to the ROIs using GIS-based software and further preprocessed through padding and scaling; however, due to some unknown causes, several missing data weeks are encountered in the database. Consequently, as the current study considers temporal models, it is deemed paramount to maintain the data sequentiality; therefore, a mean-filling approach is applied to replenish the missing data. Correspondingly, the mean is determined for the missing week-of-year of a specific location by computing the mean over all valid values of the same week for the given site in past years, contrary to finding the average of all valid data points for the whole image. The sum is further divided by the total number of years with valid values (N_t) as depicted in the following [42]:

VHI (loc,wk)

$$= \frac{\sum (\text{week-of-year 'wk' with valid values of location 'loc'})}{N_t}. \tag{1}$$

The mean-filling approach is reliable since it accommodates the seasonal tendencies for a particular week annually. Subsequently, the dataset aggregated a total of 2123 images, further split to generate the requisite datasets depicted below.

1) *Dataset - I (VHI data for peninsular India):* Postcropping and padding, the dimensions of the VHI images are (448, 578). The data are further scaled through a min–max scaler to fetch values in the range of (0, 1).

2) *Dataset - II (VHI data for Karnataka state):* Postcropping and padding the Karnataka VHI dataset in similar lines as of dataset - I, the dimensions obtained are (192, 128).

3) *Dataset - III (VHI data for Rajasthan state):* Identically to the previous datasets, postcropping and padding the Rajasthan VHI dataset, the dimensions obtained are (192, 256).

The labels are one-time-shifted compositions of the input images post scaling for all the datasets (I–III), respectively. The splitting resulted in 52 samples for testing and 2069 for training sets.

C. Rainfall Data

The lack of precipitation is a pivotal contributor to drought developments [11], constituting rainfall measurements as a critical part of drought analysis. Hence, in this work, the gridded daily rainfall data is collected from the Indian meteorological department's open-source data archive portal for the period 1981–2021 in the NetCDF format with a fine spatial resolution of $0.25° \times 0.25°$ [43], amassed from 6995 rain gauge stations.

1) Rainfall Data Preprocessing: The ROI selected for the rainfall data is the Karnataka region, cropped from the national gridded rainfall data; furthermore, its attributes, latitude, longitude, rain, and time, are used to form a 3-D interpolated raster data of the shape (timeframes, rows (latitude), columns (longitude)) with each pixel denoting the rainfall value. Also, by interpolating, resampling, and reprojecting the rainfall data into raster image data, the resolution discrepancy between the VHI and rainfall data is rectified. Subsequently, the daily rainfall data are averaged to yield a weekly representation identical to the VHI dataset and are merged with the VHI data to form the fourth dataset of the current study. The purpose of this alliance is to witness how rainfall features influence VHI-based drought analysis. Moreover, the total number of images in the rainfall dataset, 2107, is less than the satellite dataset since the rainfall data are only accessible through 2021 at the time of this study.

1) *Dataset - IV (VHI + Rainfall data for Karnataka state):* The obtained rainfall images are subsequently reshaped after padding to attain the shape (192, 128) and are scaled, reducing the rainfall values to the range of (0, 1). After a split, there are 106 samples in testing and 1999 samples in the training set. Meanwhile, the rainfall data are intertwined with the exact configuration from the ROI's VHI dataset to produce a concatenated input, with the three time-shifted VHI values as the label. Let $\mathbf{X1}_{T(192,128,1)}$ & $\mathbf{X2}_{T(192,128,1)}$ represent the matrices of a VHI and rainfall sample for a given timestamp, respectively. Subsequently, post concatenating the matrices, the data input matrix is $\mathbf{X}_{T(192,128,2)}$. The corresponding label ($\mathbf{Y}_T$) represents the three time-shifted VHI samples, i.e., equal to $\mathbf{X1}_{(T+3)}$ with the shape $\mathbf{Y}_{T(192,128,1)}$. Apropos of vegetative drought monitoring application, such a form of dataset configuration is novel.

III. PROPOSED METHODOLOGY

DL-based integration in RS is a contemporary active field with significant potential to surpass the statistical models. Similarly, in the current study, two robust DL models on satellite data are introduced that remain uninvestigated for drought analysis in such geographies.

As demonstrated in Fig. 2, the VHI and rainfall databases are cumulatively employed to develop four different datasets for three ROIs and furnished to the proposed models, P2P and BiCP2P. Furthermore, the datasets are implemented on several other ML/DL models, exhibiting the comparative study targeting the aforementioned performance matrices. Successively, the obtained outputs are color-coded into different drought severity levels.

A. Pix2Pix GAN Model

P2P, a c-GAN model that maps an observed instance x and noise vector z to the desired output y, i.e., $G : \{x, z\} \rightarrow y$, conditioned on another entity and is renowned for image-to-image translation tasks [44], is employed in this work. As exhibited in
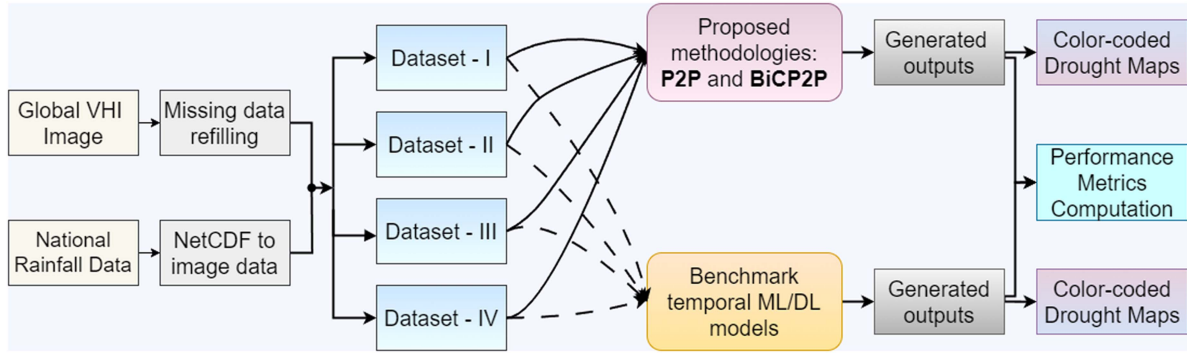
Fig. 2.   Architectural flow of the proposed methodologies on the devised datasets for drought prognosis.
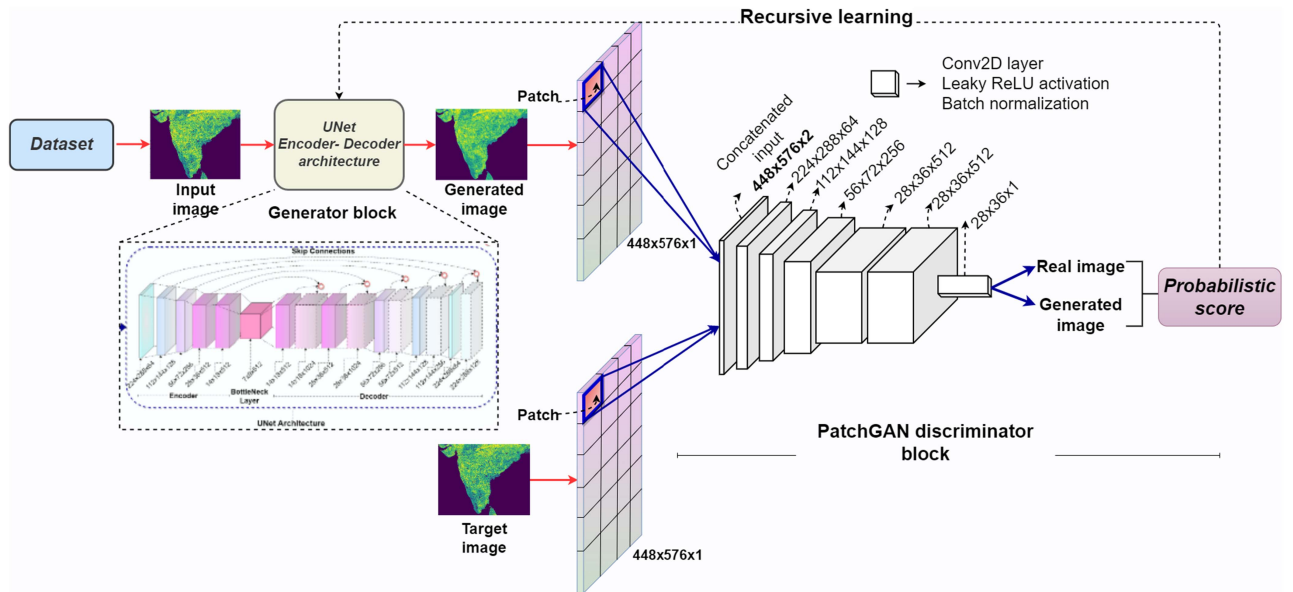

Fig. 3.   P2P architecture with UNet generator and PatchGAN discriminator.

Fig. 3, the generator (G) (further elaborated in Fig. 4) and discriminator (D) modules of P2P comprise stacked convolutional layers, followed by normalization and pooling layers; a similar strategy is adopted in this work.

1) Generator: Fig. 4 illustrates the encoder–decoder form of the UNet architecture of the P2P generator block that contains skip connections to retain low-level information over the layers. Meanwhile, as the encoder incrementally applies downsampling layers till the bottleneck layer is attained, the decoder performs upsampling to generate the final output representation. Additionally, in the UNet design, the input and output share identical spatial representation [36], where each layer k and layer $(m - k)$, m constituting the total number of layers, are connected by the skip connections, and the channels extant at these two tiers are concatenated. In this work, the encoder is structured with succeeding blocks of convolutional layers equipped with constant filters of size (4, 4) and strides of (2, 2), wherein the feature dimensions W and L (width, length) are successively halved, and the number of filters doubles sequentially from 64 to 512. Conversely, the decoder performs the reverse operation of the encoder.

2) Discriminator: The P2P model embodies a PatchGAN discriminator, which processes the $N \times N$ patch, a hyperparameter to arbitrate if the patch under consideration is real or artificial instead of the complete image (see Fig. 3). Moreover, the discriminator inheres a deep CNN block configured to build a receptive field that can accord any smaller or larger dataset as patches, further improving generalization. In this work, $N = 1$ is selected, which projects onto a receptive field of 70×70; subsequently, convolution is applied on patches by the discriminator across the image and computes the probabilistic loss over the assigned paired images (target image, generated image). Finally, a feature map is produced at the discriminator chain and averaged to provide a single score [36] as the discriminator loss, which is passed to the generator for more realistic data synthesis, as demonstrated in Fig. 3.

3) Implementation and Training of P2P GAN: As depicted in Fig. 3, the input image from the dataset is supplied to the generator block, which yields a future representation of the conveyed sample; the generated and ground truth images are further provisioned to the discriminator block, which computes a probabilistic score to determine the actual image among the
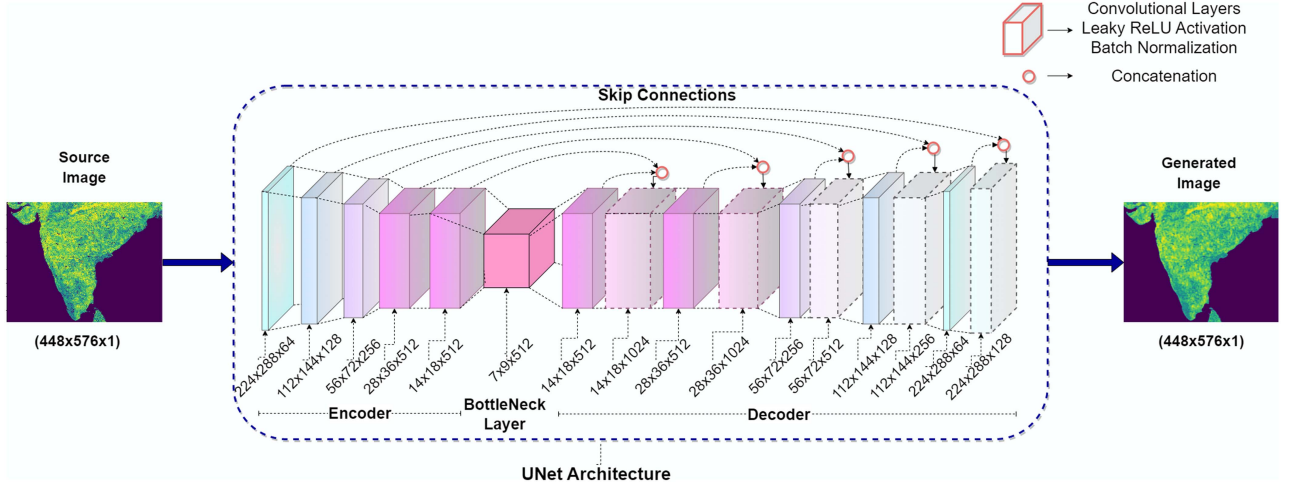
Fig. 4. Generator architecture of P2P: A UNet architecture with skip connections and mirrored encoder–decoder layers. The dotted blocks in the decoding route denote concatenated outputs from the skip connections.

TABLE III
NOTATIONS USED IN LOSS EQUATIONS OF C-GAN

Symbol	Description
G	Generator model
D	Discriminator model
z	Random noise element
x	Real image
y	Ground-truth or label image
$G(x, z)$	Image generated by generator (fake image)
$D(x, G(x, z))$	Discriminator's output when the generated image is an input
$D(x, y)$	Discriminator's output when the real image is an input

two. The training is iteratively executed until the probabilistic score nears 0.5 and the generated outcomes emerge realistic, followed by segregation into various drought levels to examine the ROI drought condition thoroughly.

The P2P model training is consummated over the generative adversarial and discriminator losses given the real and fake images. The c-GAN objective function ($\mathcal{L}_{c-GAN}(G, D)$) is a marginally modified version of the simple GAN model

$$\mathcal{L}_{c-GAN}(G, D) = \mathrm{E}_{x,y}[\log D(x, y)] \\ + \mathrm{E}_{x,z}[\log(1 - D(x, G(x, z)))]. \quad (2)$$

As illustrated in (2), the objective function of P2P is formulated as an average log probability computed for the generator and discriminator. Table III displays the notations used in the equations.

In (2), the log probability $\mathrm{E}_{x,y}[\log D(x, y)]$ denotes the average probability of D when the real image is input, and the log probability $\mathrm{E}_{x,z}[\log(1 - D(x, G(x, z)))]$ denotes the average probability of D when input provided is the generated image. G, i.e., the generator attempts to reduce the combined loss function [36] whereas D, i.e., the discriminator attempts to maximize the loss function. Along with minimizing the adversarial loss of (2), the generator in c-GAN must also beget a visual perception closest to the labels supplied; therefore, $L2$ loss ($\mathcal{L}_{L2}(G)$) is estimated amid real label y and produced image $G(x, z)$ as revealed in the following:

$$\mathcal{L}_{L2}(G) = \mathrm{E}_{x,y,z}\left[\|y - G(x, z)\|_2\right]. \quad (3)$$

Resultantly, the following manifests the total loss or objective function ($\mathcal{L}_{\text{total}}(G)$) for c-GAN:

$$\mathcal{L}_{\text{total}}(G) = \mathcal{L}_{c-GAN}(G, D) + \mathcal{L}_{L2}(G). \quad (4)$$

Subsequently, the following implies the generator's dual min–max objective function (G^*), where it pursues to reduce the loss while the adversarial discriminator attempts to boost it; λ designates a tuneable hyperparameter

$$G^* = \arg \min_G \max_D \{\mathcal{L}_{c-GAN}(G, D) + \lambda \mathcal{L}_{L2}(G)\}. \quad (5)$$

The generator employs a weighted (λ) mixture of both losses (adversarial and $L2$) ranging in the interval of [0,100] in this work. Moreover, the loss function computation is gradual for the generator since it learns via the discriminator, whereas the discriminator is explicitly trained and learns rapidly compared to the generator. Consequently, during training, the discriminator's training loss function is downsized (usually halved) to comply with the generator's training pace.

Contrary to basic GAN models, the generator is not supplied with a random noise vector; instead, the input is procured from the source domain, and the randomness (z) is instilled through the architecture's dropout layers. As a corollary, the source image is injected into the generator, which produces artificial samples recursively during training, following which the discriminator consumes a paired image (target image, generated image). Let $\mathbf{X}$ represent the paired dataset array as the P2P model accepts input in the form of paired images (source image, target image), where data points are equipped as a pair of (x_t, y_t) where each $x_t, y_t \in \mathbf{X}$ and $y_t = x_{t+1}$, i.e., one time-stamp shifted. Consequently, the created dataset is of the format: $(\text{X\_train}_{(2069,448,576,1)}, \text{y\_train}_{(2069,448,576,1)})$ and $(\text{X\_test}_{(52,448,576,1)}, \text{y\_test}_{(52,448,576,1)})$. Unlike standard forecasting DL models, no temporal sampling is applied in the present model, and the training imbibes a predetermined number of samples, n_samples (tunable hyperparameter), concurrently from the paired train dataset, acclimated to three in the current study.
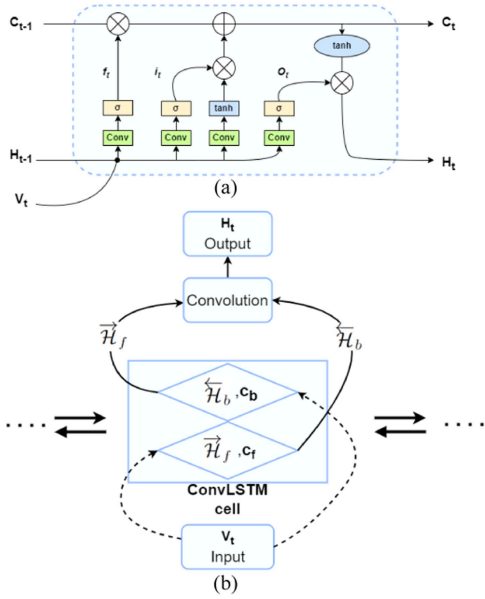
Fig. 5. Inner architecture of (a) ConvLSTM and (b) BiConvLSTM module [45].

B. BiConvLSTM-Pix2Pix GAN Model (BiCP2P)

The BiCP2P model, a modified variant of the basic P2P model, is the second suggested model of this work, imbibing an analogous model architecture as the P2P model (see Fig. 3), except for the distinction in skip connection establishment. Furthermore, the simple P2P GAN concatenates the layer from the downsampled encoding path to the preceding upsampled layer of the decoding path; however, interjecting a BiConvLSTM block in the concatenation assists in coupling the layers in a nonlinear manner to further enhance the features [28], [29]. The encoding path retains higher-resolution feature maps, whereas the decoding path gains by extracting semantic information. Additionally, dense convolutions are employed after the contracting route to curb the problem of vanishing/exploding gradient and to retain a rich collection of different features, and the collected outputs further proceed to the expanding route. Moreover, the feature map devised by the encoding path at layer k and the one induced by the preceding convolutional layer at layer $(m-k)$ is input into the BiConvLSTM block for nonlinear concatenation, asserting spatial relationships, which is advantageous when dealing with ST data.

1) BiConvLSTM Model: Functioning with ST data designates it imperative to acquire a comprehensive understanding of the characteristics, facilitated by employing BiConvLSTM by conducting back training alongside forward learning, as exhibited in Fig. 5. Moreover, BiConvLSTM's learning technique is comparable to the ConvLSTM model, except that it incorporates both forward and backward sequences during training instead of just forward learning [28], [45]. The temporal input sequence is reversed and fed as the backward sequence to the ConvLSTM block to attain the ricocheted sequence outputs. Also, ConvLSTM, similar to LSTM, controls information flow through self-parametrized gates; however, transitions are convolutional

for input-to-state and within-state in the ConvLSTM model [46]. Input (i_t), output (o_t), and forget (f_t) gates constitute the ConvLSTM architecture. The inputs $V_1, V_2, \ldots V_t$, which in the current instance depicts the feature maps from the encoded and decoded route, cell states $C_1, C_2, \ldots, C_t$, i.e., the retained memory, and $H_1, H_2, \ldots H_t$ represent the hidden states, are passed via "*sigmoid*" ($\sigma(.)$) and "*tanh*" activations. W_{v*}, W_{h*}, and W_{c*} represent the convolutional kernels for input, hidden layers, and memory cells, and b_i, b_c, and b_f denote the biases. The input gate i_t permits input information to enter, c_t symbolizes memory cells that store current information, f_t determines whether the data should be forgotten or retained, and o_t or the output gate connects the final output to H_t. These ConvLSTM layers may be stacked to build forecasting applications [46], [47]

$$i_t = \sigma \left(W_{vi} * V_t + W_{hi} * H_{t-1} + W_{ci} \odot C_{t-1} + b_i \right) \quad (6a)$$

$$f_t = \sigma \left(W_{vf} * V_t + W_{hf} * H_{t-1} + W_{cf} \odot C_{t-1} + b_f \right) (6b)$$

$$C_t = f_t \odot C_{t-1} + i_t \odot \tanh \left(W_{vc} * V_t + W_{hc} * H_{t-1} + b_c \right) \quad (6c)$$

$$o_t = \sigma \left(W_{vo} * V_t + W_{ho} * H_{t-1} + W_{co} \odot C_t + b_c \right) \quad (6d)$$

$$H_t = o_t \odot \tanh \left(C_t \right). \quad (6e)$$

Consecutively, the future cell output of a particular cell is determined by the data input and the previous state of the surrounding cells. The equations for ConvLSTM are demonstrated in (6a)–(6e), where the convolution operation is represented by "$*$", and "$\odot$" expresses the Hadamard product. The equations for forward and backward calculations for the BiConvLSTM model are equivalent. In furtherance of calculating the combined output, the ConvLSTM block's forward and backward outputs are merged in the following:

$$\mathbf{Y_t} = \tanh \left(W_y^{\overrightarrow{\mathcal{H}}} * \overrightarrow{\mathcal{H}}_f + W_y^{\overleftarrow{\mathcal{H}}} * \overleftarrow{\mathcal{H}}_b + b \right). \quad (7)$$

In (7), $\overrightarrow{\mathcal{H}}_f$ and $\overleftarrow{\mathcal{H}}_b$ denote tensors for the hidden state in the forward and backward direction, respectively. Also, in BiConvLSTM, the final output (Y_t) is obtained by convoluting these hidden sequences with their respective kernels ($W_y^{\overrightarrow{\mathcal{H}}}, W_y^{\overleftarrow{\mathcal{H}}}$) as depicted in Fig. 5(b). The output Y_t will be relayed along the expanding route of the UNet architecture. Subsequently, the dense convolutions adopted in the final layers of the encoding path incorporate all the preceding feature maps coupled as input, eliminating any duplicate features recorded in earlier layers.

2) Implementation and Training of BiCP2P: The P2P and BiCP2P models adorn structural resemblance and hold identical objective functions (4)–(5), which remain unaltered by the distinct concatenation adjustments, along with employing similar training parameters. For a fair comparison, the hyperparameter settings for both models are left unchanged. Furthermore, the implementation process adopted is also analogous to the P2P model, with the identical input dataset supplied to the model.

TABLE IV
DL MODELS CONFIGURATION

DL Model	No. of filters (Kernel size=3)	Activation/ Optimizer
ConvLSTM+Conv3D	8, 16, 64, 128, 64, 16	'ReLu' / 'SGD'
ConvLSTM+Conv2D	8, 32, 128, 64, 8	'ReLu' / 'SGD'
Conv3D	8, 8, 16, 1	'ReLu' / 'SGD'
1D-CNN	64, 50, 258048	'ReLu' / 'Adam'
BiLSTM	50, 1200, 200, 258048	'ReLu' / 'Adam'

TABLE V
COLOR-CODING TO SEGMENT INTO DROUGHT SEVERITY LEVELS

Pixel values	Value for colormap	Drought severity
> 80	255	Healthy vegetation
80 − 60	128	Normal
59 − 40	64	Light dry
39 − 20	32	Moderate drought
< 20	0	Extreme drought

IV. COMPARATIVE ANALYSIS AND MODEL OPTIMIZATION

This section discusses the comparison models employed for model performance analysis. Furthermore, the procedures for fine-tuning and optimization have been outlined.

A. Reference Models for Comparative Studies

Various ML/DL-based models, prevalent in temporal data handling, are applied to produce qualitative and quantitative comparisons. The qualitative comparison is demonstrated through color-coded drought maps, and the quantitative comparison is accomplished by analyzing the model performance metrics. The color scheme is consistent with the values in Table II.

1) *DL Models:* The DL models exercised for comparison are outlined in Table IV. Moreover, temporal sampling is employed to supply data into the DL models. For this study, two-time sampling is adopted, with the label being a comparable single-time-shifted version of the input. The layer outputs of the models are standardized through group normalization. Also, in the 1-D-CNN and BiLSTM models, the data dimensions (width, height, and depth) are flattened and applied with the last layer of the models possessing nodes equal to the flattened shape, as annotated in Table IV.

2) *ML Models:* KNN, decision tree (DT), RF, and extreme gradient boosting (XGBoost) are the ML regressor models applied and compared in the present work. Some of these ML models consumed considerably larger memory than the DL models, guaranteeing DL models an advantage over the ML models.

3) *Ensemble Models:* A few ensemble-based models constructed using the aforementioned ML/DL models are also evaluated. ConvLSTM+Conv3-D+DT and ConvLSTM+Conv3-D+P2P ensemble models are implemented in the current work.

B. Model Optimization and Tuning

For a suitable paralleling, it is imperative to acquire the best outcomes [23]; consequently, the implemented models are optimized to demonstrate the best performances in the respective geographies for all the datasets. Correspondingly, the ML models have been ameliorated by hyper-tuning the parameter arguments; for KNN, the number of nearest neighbors (k) is modified (in the range of 2−5), DT, RF, and XGBoost form a part of the bagging techniques and are optimized by tuning the hyperparameters such as the number of trees (in the range

1−3), maximum depth (in the range 1−2), and the number of estimators (in the range 1−3). Since the datasets are enormous, large hyperparameter values are deemed computationally costly and, hence, are restricted to nominal counts. Similarly, for the DL models, the optimal performance is achieved by modifying the number of layers, nodes per layer and epochs, the optimizer, and activation functions. The number of layers has been rendered in the range of 3−7 layers, with the number of nodes varying based on the dataset size and epochs in the range of 20−50. The activation functions have oscillated between $ReLU$ and $Sigmoid$, out of which $ReLU$ outperformed the latter across all cases. Subsequently, the optimization functions examined include SGD and $Adam$ optimizers for which the learning rates have been varied in the range of 0.01−0.2.

V. RESULTS AND DISCUSSIONS

The present section exhibits the comprehensive simulation results of the proposed DL models for drought prediction. The results are unscaled to obtain their true range of VHI values, i.e., [0, 100]. Furthermore, the ROI is segmented into various drought severity zones as per Table II, and color-coding is performed to acquire the drought maps as per Table V. All computations are carried out on a 40 Gb NVIDIA (DGX) GPU and 16 Gb NVIDIA RTX (A4000) GPU graphics card.

A. Performance Analysis Among Models

Performance metrics for all the models across all datasets are derived, and a quantitative comparison is presented. For each model, MSE, MAE, and R2 scores are computed with the actual label and generated output supplied to it.

1) *Mean Squared Error (MSE):* MSE determines the closeness of the regression line to a set of points; therefore, lower MSE values represent accurate forecasting.

2) *Mean Absolute Error (MAE):* MAE represents the absolute anomaly amidst the points and lines irrespective of their direction; therefore, lower MAE values demonstrate accurate prediction.

3) *Coefficient of Determination (R2 Score):* The R2 score determines the proportion of observed variance to the total variance present in the data. The R2 score ranges from 0 to 1, with the larger value denoting an accurate regression model fit.

Table VI describes the formulae for performance metrics in which the notations depict i as the ith input sample, $\widehat{y}_i$ as the expected output value, y_i as the real label value, $\bar{y}$ denoting the mean of the observed true value and T as the total number of samples.

TABLE VI
METRIC FORMULAE

Metric	Formulae
MSE	$\frac{1}{T} \sum_{i=1}^{T} (y_i - \widehat{y_i})^2$
MAE	$\frac{1}{T} \sum_{i=1}^{T} |y_i - \widehat{y_i}|$
R2 score	$1 - \frac{\sum_i (y_i - \hat{y}_i)^2}{\sum_i (y_i - \overline{y})^2}$

B. P2P Model Training and Derived Metrics

The current subsection presents the drought assessment study implementing the P2P model on the four aforementioned datasets. As conferred earlier, paired datasets are given to the P2P model during training, which is performed in batches_per_epoch, equivalent to (length of training input/ batch_size) with epochs = 10 and batch size = 1. Additionally, the number of steps for which the training ensues is defined as $n_steps = $ batch_per_epoch $*$ epochs, where batch_per_epoch and the number of epochs are hyperparameters tuned to identify the best fit. Subsequently, the model is considered well trained if the discriminator's loss for real, D_loss1 [see Fig. 6(a)] and generated images, D_loss2 [see Fig. 6(b)] docks at a median approximate probabilistic loss of 0.5, with the images being nearly indistinguishable. The generator loss also abridges to a meager value over the iterations, as observed in Fig. 6(e).

C. BiCP2P Model Training and Derived Metrics

The current subsection stages the drought assessment study implementing the BiCP2P model on the datasets. Notably, the training parameters for BiCP2P and P2P remain identical for the present study. Fig. 6(c)–(d) and (f) displays the training curves for the discriminator and generator, respectively. Correspondingly, the generator loss exhibits a declining trend with occasional noisy spikes in between, which may be ascribed to the conditional learning of GAN. As envisaged, the discriminator losses are nearing their optimal saturation threshold, i.e., 0.5.

D. Comprehensive Drought Assessment Among Reference Models

A multitude of ML and DL models are studied to provide a comprehensive comparison with the proposed models. The quantitative comparison entailed examining the metric scores, whereas the qualitative comparison implicated assessing how precisely the generated drought maps approximate the envisioned drought map for the ROI.

1) Quantitative Comparison Among Models for All Datasets: Table VII depicts the performance metrics comparison for dataset - I, wherein GAN-based models outperformed other reference models in forecasting the future VHI values over the ROI. Conspicuously, the P2P model acquired a mean R2 score of 0.971 and a maximum of 0.986 on the test samples with loss measures MSE and MAE reduced to 0.0016 and
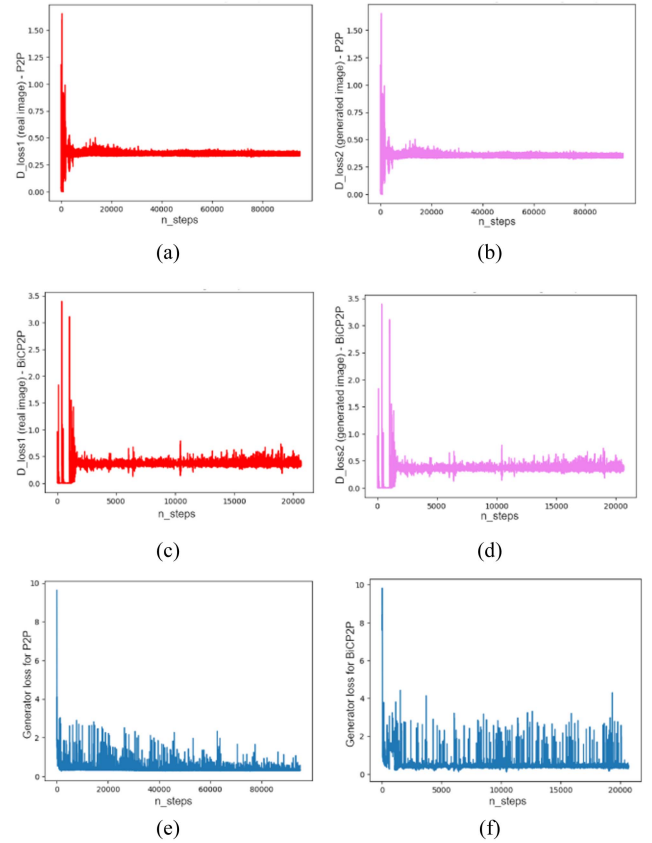

Fig. 6. Training losses for model. (a) P2P: D_loss1 when input is a real image. (b) P2P: D_loss2 when input is generated image. (c) BiCP2P: D_loss1 when input is a real image. (d) BiCP2P: D_loss2 when input is generated image. (e) Generator training loss for P2P. (f) Generator training loss for BiCP2P.

TABLE VII
METRIC COMPARISON AMONG ALL MODELS (DATASET - I)

Model	Epochs/steps	Mean R2	Max R2	Mean MSE	Mean MAE
P2P	80K steps	**0.971**	**0.986**	**0.0016**	**0.020**
BiCP2P	80K steps	**0.963**	**0.98**	**0.0021**	**0.0239**
ConvLSTM+Conv3D+P2P	–	0.952	0.971	0.0029	0.0365
KNN regressor	–	0.91	0.95	0.0063	0.038
ConvLSTM+Conv3D	30	0.88	0.93	0.0076	0.0615
ConvLSTM+Conv3D+DT	–	0.799	0.844	0.0142	0.0733
RF	–	0.77	0.80	0.0168	0.0692
BiLSTM	30	0.71	0.76	0.0205	0.0766
1D-CNN	40	0.70	0.75	0.0216	0.0799
ConvLSTM+Conv2D	40	0.647	0.712	0.025	0.088
Conv3D	50	0.46	0.55	0.0404	0.1504
DT regressor	–	0.46	0.58	0.102	0.0369
XGBoost	–	0.22	0.36	0.0431	0.1887

In order to highlight the metric scores obtained by our proposed models (P2P and BiCP2P) and emphasize their superior performance compared to other models, the numbers are marked in bold.

0.020, respectively. Similarly, the BiCP2P model cultivated considerable performance metrics, although it underperformed marginally compared to the P2P model. Peninsular India represents an enormous geographic landmass, and on such a topology, the generative models capably traced the vegetation properties better than other recognized ML/DL models, granting them a competitive advantage that renders them enticing for large-scale forecasting applications.

Besides, the proposed models excelled in performance compared to the reference models, as validated through the metrics obtained by other state-of-the-art temporal models, demonstrating the less efficient predictions through models such as

TABLE VIII
METRIC COMPARISON AMONG ALL MODELS (DATASET - II)

Model	Epochs/steps	Mean R2	Max R2	Mean MSE	Mean MAE
P2P	80K steps	**0.95**	**0.96**	**0.0018**	**0.023**
BiCP2P	80K steps	**0.9462**	**0.956**	**0.0021**	**0.0254**
KNN regressor	–	0.93	0.95	0.0058	0.040
ConvLSTM+Conv3D+P2P	–	0.92	0.93	0.0048	0.045
1D-CNN	40	0.88	0.91	0.0077	0.0499
ConvLSTM+Conv3D+DT	–	0.86	0.915	0.0100	0.0626
ConvLSTM+Conv3D	30	0.83	0.93	0.0131	0.0771
DT regressor	–	0.81	0.95	0.017	0.071
RF	–	0.81	0.85	0.0194	0.0796
BiLSTM	30	0.78	0.81	0.0182	0.0769
XGBoost	–	0.30	0.36	0.0414	0.1835
Conv3D	50	0.29	0.35	0.060	0.19
ConvLSTM+Conv2D	40	0.22	0.37	0.075	0.179

In order to highlight the metric scores obtained by our proposed models (P2P and BiCP2P) and emphasize their superior performance compared to other models, the numbers are marked in bold.

TABLE IX
METRIC COMPARISON AMONG ALL MODELS (DATASET - III)

Model	Epochs/steps	Mean R2	Max R2	Mean MSE	Mean MAE
P2P	80K steps	**0.92**	**0.94**	**0.0018**	**0.0235**
BiCP2P	80K steps	**0.92**	**0.938**	**0.0021**	**0.024**
ConvLSTM+Conv3D+P2P	–	0.89	0.91	0.0044	0.0388
KNN regressor	–	0.89	0.94	0.0077	0.045
ConvLSTM+Conv2D	40	0.80	0.88	0.0112	0.0604
ConvLSTM+Conv3D+DT	–	0.80	0.85	0.0110	0.061
ConvLSTM+Conv3D	30	0.77	0.84	0.0134	0.0684
RF	–	0.76	0.87	0.0172	0.0739
DT regressor	–	0.75	0.86	0.0179	0.075
1D-CNN	40	0.73	0.81	0.0161	0.0711
BiLSTM	30	0.67	0.81	0.0197	0.0799
Conv3D	50	0.59	0.72	0.0273	0.108
XGBoost	–	0.248	0.35	0.0413	0.1832

In order to highlight the metric scores obtained by our proposed models (P2P and BiCP2P) and emphasize their superior performance compared to other models, the numbers are marked in bold.

TABLE X
METRIC COMPARISON AMONG ALL MODELS (DATASET - IV)

Model	Epochs/steps	Mean R2	Max R2	Mean MSE	Mean MAE
P2P	80K steps	**0.93**	**0.95**	**0.0033**	**0.032**
BiCP2P	80K steps	**0.94**	**0.95**	**0.0042**	**0.033**
ConvLSTM+Conv3D+P2P	–	0.91	0.93	0.0054	0.045
ConvLSTM+Conv2D	40	0.88	0.91	0.0591	0.0110
KNN regressor	–	0.87	0.95	0.0011	0.059
ConvLSTM+Conv3D+DT	–	0.85	0.93	0.0100	0.060
ConvLSTM+Conv3D	30	0.84	0.91	0.0114	0.067
RF	–	0.79	0.85	0.0191	0.0799
DT regressor	–	0.76	0.93	0.022	0.080
1D-CNN	40	0.76	0.81	0.0188	0.0799
BiLSTM	30	0.74	0.80	0.0226	0.0863
Conv3D	50	0.46	0.55	0.0404	0.1504
XGBoost	–	0.33	0.29	0.0406	0.1808

In order to highlight the metric scores obtained by our proposed models (P2P and BiCP2P) and emphasize their superior performance compared to other models, the numbers are marked in bold.

ConvLSTM-based methods, RF, and the least-performing XG-Boost, which fails to provide a good prognosis on the peninsular Indian geography. A similar excellent performance is witnessed for dataset - II through Table VIII with the suggested models delivering superior metric scores, such as mean and maximal R2 score, MSE, and MAE of 0.95, 0.96, 0.0018, and 0.023, respectively, for P2P model.

Analogously, the BiCP2P also outshines other reference models; however, it demonstrates minor degradation in prediction accuracy (in terms of the R2 score) and increased loss values compared with P2P, whereas the XGBoost model proves unfit for drought prediction with the provided input features. Comparatively, the ConvLSTM-based models performed suboptimally and could not surpass the performance of the P2P model. Furthermore, the results for dataset - III accentuate the high-performance caliber of the recommended models, as shown in Table IX, with prominent metrics of mean and maximum R2, MSE, and MAE as 0.92, 0.94, 0.0018, and 0.0235 for the P2P model. Interestingly, for the Rajasthan topology, the BiCP2P model matches the P2P model performance, while other reference models perform unfavorably with lower R2 scores and larger loss values. Also, the computational training cost for the proposed models, on the available resources for this research, is considerably lower than other models.

Dataset - IV, comprising mixed features of satellite and meteorological data, further validates the excellency of the proposed models in predicting future VHI values. As demonstrated in Table X, the P2P model gained mean and maximal R2 score, MSE, and MAE of 0.93, 0.95, 0.0033, and 0.032, respectively. Contrarily, the metrics obtained for the traditional models are insufficiently accurate compared to our proposed

models, as reflected by their inferior metric scores. Moreover, the ConvLSTM-based models require more parameters and consume increased computational time, delivering unsatisfactory outcomes. Also, the ML models, such as RF, DT, and XGBoost, consumed exceptionally long training durations and produced unsatisfactory results, with the XGboost possessing the most inconsequential metrics, implying that the randomness feature of the bagging techniques is unfit for future prediction on the presented datasets.

2) Qualitative Comparison Among Models: Fig. 7 delineates drought maps, color-coded as per the drought severity levels (see Table V), generated by the proposed and referenced models for comparative study for dataset - I. Fig. 7(a) depicts the expected drought mapping for comparison with other models' outputs. Consecutively, Fig. 7(b) and (c) epitomizes the drought maps yielded through the proposed models P2P and BiCP2P, respectively, validating outstanding performance metrics compared with the reference models' outputs shown in Fig. 7(d)–(n). Following Table II, the dark green regions in the drought maps illustrate prominent vegetation cover and less drought-prone. Furthermore, as can be observed, the drought maps spawned by other models do not justify their prominence for future scenario prediction and have significant alterations compared to the expected output; for instance, the drought map generated by XGBoost, fails to identify the ROI regions efficiently, and similarly, the ConvLSTM models also fail.

Fig. 8 outlines drought maps rendered by the proposed and referenced models for dataset - II. Fig. 8(b) and (c) exemplifies the drought maps generated through the proposed models P2P and BiCP2P, respectively. As can be inferred, for the proposed models, the resemblance of ground truth [see Fig. 8(a)] and generated maps are unduly precise compared to reference models [see Fig. 8(d)–(n)]. Moreover, ML methods such as DT [see Fig. 8(j)] are inept in performance, as inferred through the drought maps validating their inefficiency for drought forecasting applications. Similarly, preferred DL-based models for time-series data processing, such as ConvLSTM+Conv3D [see Fig. 8(d)], are unable to comprehend the data complexity correctly. Additionally, the satisfactory performance of the suggested models on both a smaller region such as Karnataka and for peninsular India, as seen priorly, justifies its prediction potential. Apparently, the drought severity demonstrated through color-coding can aid in identifying the places having more probability of drought events.
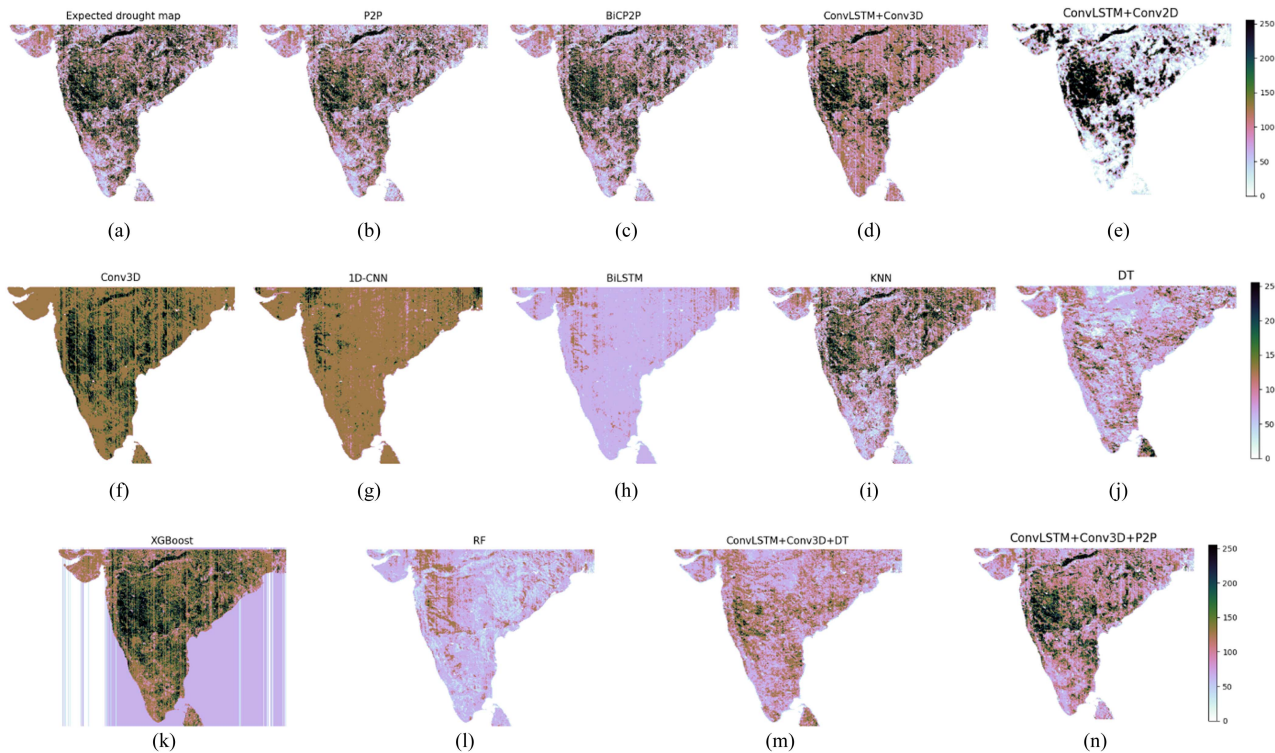
Fig. 7.   Comparison of drought maps generated through the proposed and reference models for dataset - I. (a) Expected drought map. (b) P2P. (c) BiCP2P. (d) ConvLSTM+Conv3-D. (e) ConvLSTM+Conv2-D. (f) Conv3-D. (g) 1-D-CNN. (h) BiLSTM. (i) KNN. (j) DT. (k) XGBoost. (l) RF. (m) ConvLSTM+Conv3-D+DT. (n) ConvLSTM+Conv3-D+P2P.
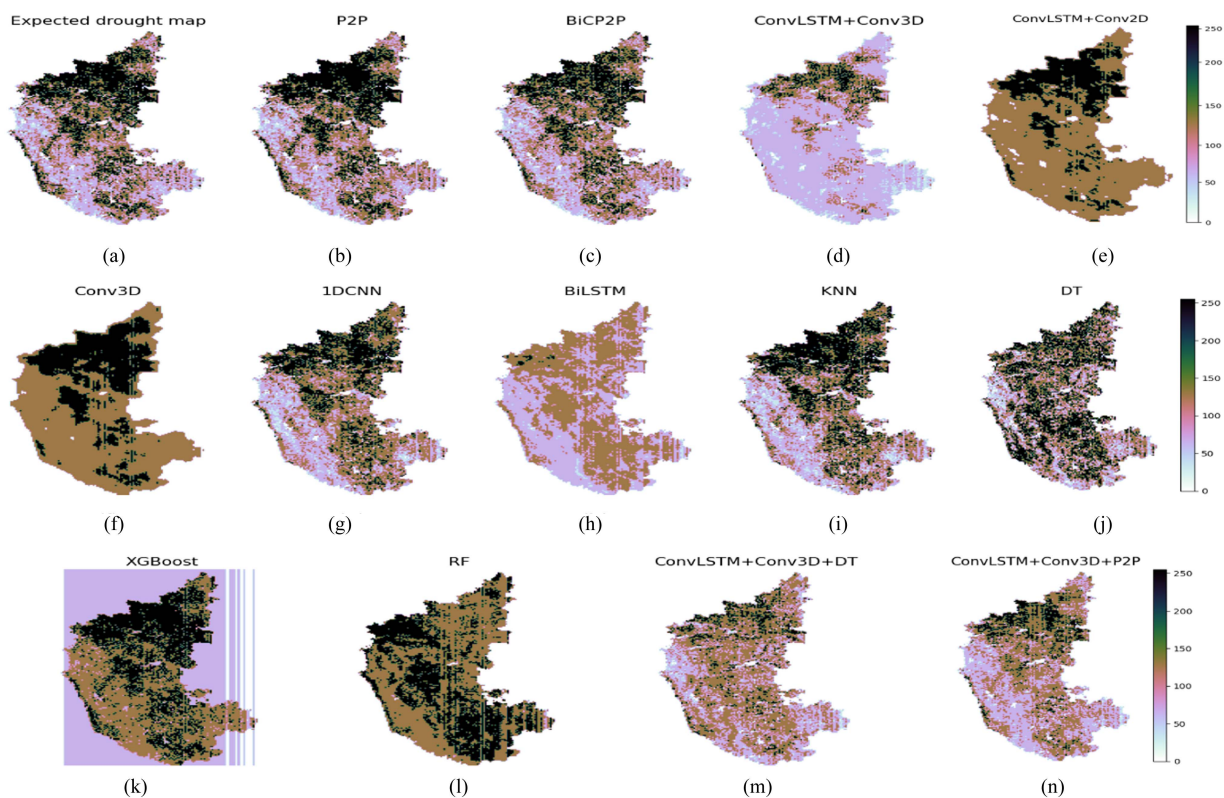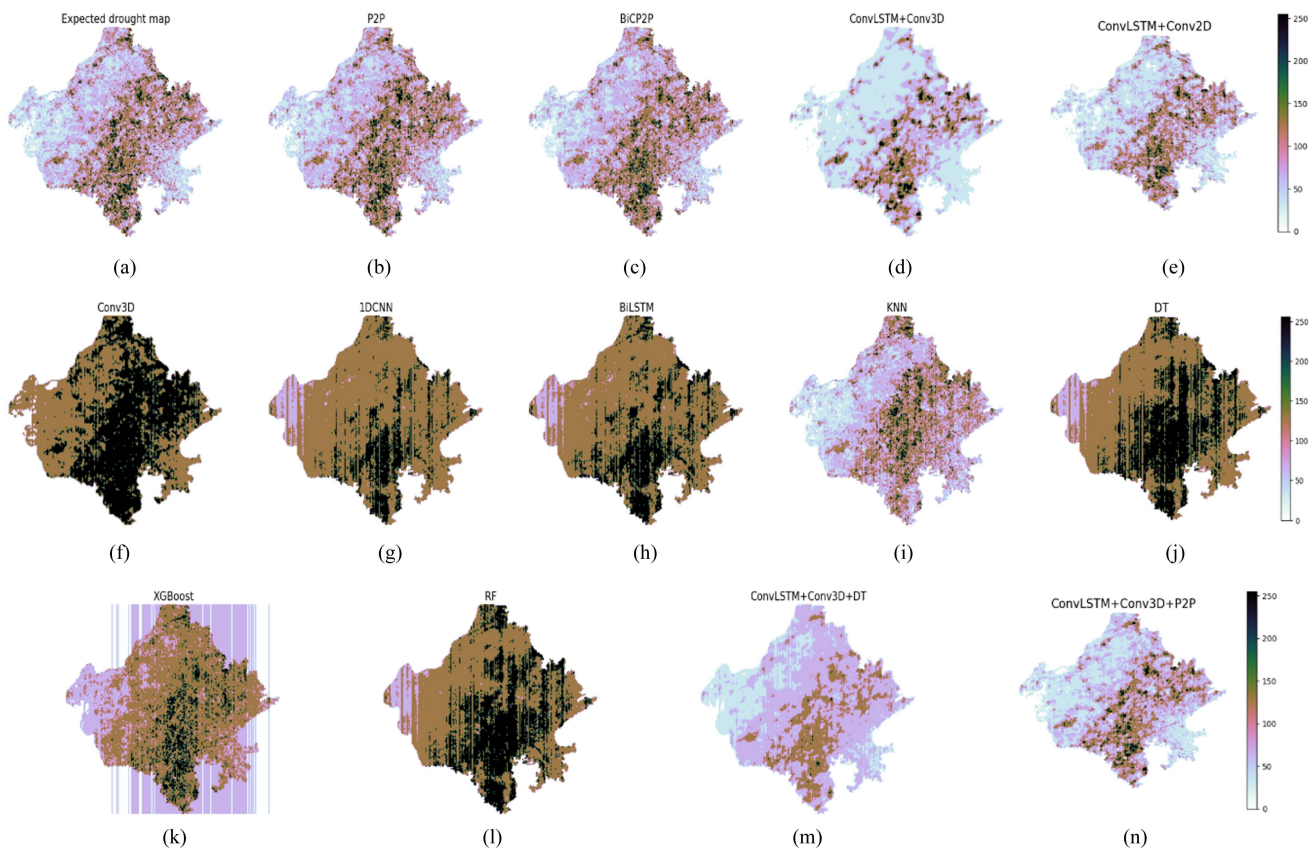

Fig. 8.   Comparison of drought maps generated through the proposed and reference models for dataset - II. (a) Expected drought map. (b) P2P. (c) BiCP2P. (d) ConvLSTM+Conv3-D. (e) ConvLSTM+Conv2-D. (f) Conv3-D. (g) 1-D-CNN. (h) BiLSTM. (i) KNN. (j) DT. (k) XGBoost. (l) RF. (m) ConvLSTM+Conv3-D+DT. (n) ConvLSTM+Conv3-D+P2P.

Fig. 9. Comparison of drought maps generated through the proposed and reference models for dataset - III. (a) Expected drought map. (b) P2P. (c) BiCP2P. (d) ConvLSTM+Conv3-D. (e) ConvLSTM+Conv2-D. (f) Conv3-D. (g) 1-D-CNN. (h) BiLSTM. (i) KNN. (j) DT. (k) XGBoost. (l) RF. (m) ConvLSTM+Conv3-D+DT. (n) ConvLSTM+Conv3-D+P2P.

Correspondingly, the drought maps obtained by the suggested and reference models for the third dataset are demonstrated in Fig. 9(b)–(c) and (d)–(n), respectively. Remarkably, even for a drier region such as Rajasthan, with significant variations in the greenery, the suggested models display promising prediction results. As can be seen, the northwest regions appear comparatively drier as per the color-coding scheme, which covers the Thar desert topology of the state and has been correctly classified by the proposed models. Conversely, other renowned models do not show sufficient resemblance with the ground truth image [see Fig. 9(a)] with the worst performance demonstrated by XGBoost. Also, the ConvLSTM-based models inadequately perform over the target geography.

Furthermore, Fig. 10 exhibits drought maps stemmed by the proposed and reference models for comparative study on dataset - IV, wherein the features of rainfall and satellite-data-derived VHI values are collated. Fig. 10(b) and (c) presents the drought maps induced through the proposed models P2P and BiCP2P, respectively. The presented models reflect outstanding results for dataset - IV and can track the intricate changes in the dataset more precisely than the reference models. Besides, the insufficient resemblance of reference models' drought maps [see Fig. 10(d)–(n)] concludes that the mixed features input is not well-comprehended by the models and hence, is unfit for the research objective of this article.

Additionally, the drought severity levels obtained through the rendered drought maps by the proposed models can further be studied to understand the trend and pattern of drought occurrences. As per the study conducted in [48], India faced one of the worst droughts in 2000. To further infer from the generated drought maps, the outputs for weeks 24 to 31 are observed in this study, which marks an adequate season for many crops, for the drought year 2000. The outcomes for a nondrought year, conformed as 2017, are further displayed for the same weeks to contrast the two drought maps and validate the presence of drought in the year 2000.

Definitively, Fig. 11 reveals the severe differences between the green cover for the same weeks in a drought year and a nondrought year. Fig. 11(a) and (b) peculiarly demonstrate the region affected under moderate to extreme drought, as referred to in Table V. Moreover, the whiter shades demonstrate a lack of greenery, as a result of which the VHI value dropped for the region when it was drought-hit. Conversely, for the drought maps of the year 2017, a healthy green cover (depicted by hues of brown) over the western ghat belt of the peninsular region can be noted from Fig. 11(c) and (d). Furthermore, P2P and BiCP2P models validate their efficacy by distinctly predicting the maps for drought and nondrought years. Convincingly, such efficient drought segmentation further emphasizes the need to perform such prediction tasks more frequently to tackle future
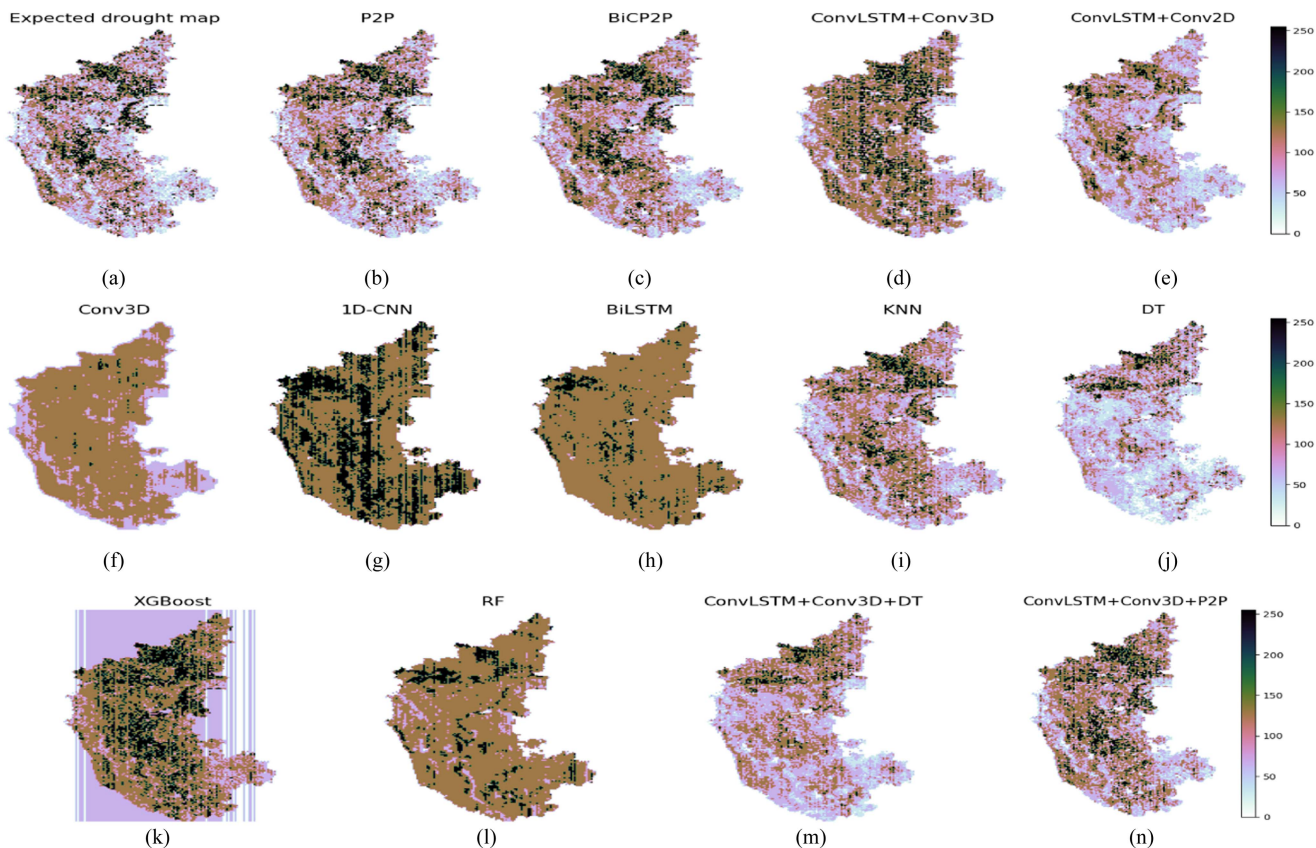
Fig. 10. Comparison of drought maps generated through the proposed and reference models for dataset - IV. (a) Expected drought map. (b) P2P. (c) BiCP2P. (d) ConvLSTM+Conv3-D. (e) ConvLSTM+Conv2-D. (f) Conv3-D. (g) 1-D-CNN. (h) BiLSTM. (i) KNN. (j) DT. (k) XGBoost. (l) RF. (m) ConvLSTM+Conv3-D+DT. (n) ConvLSTM+Conv3-D+P2P.
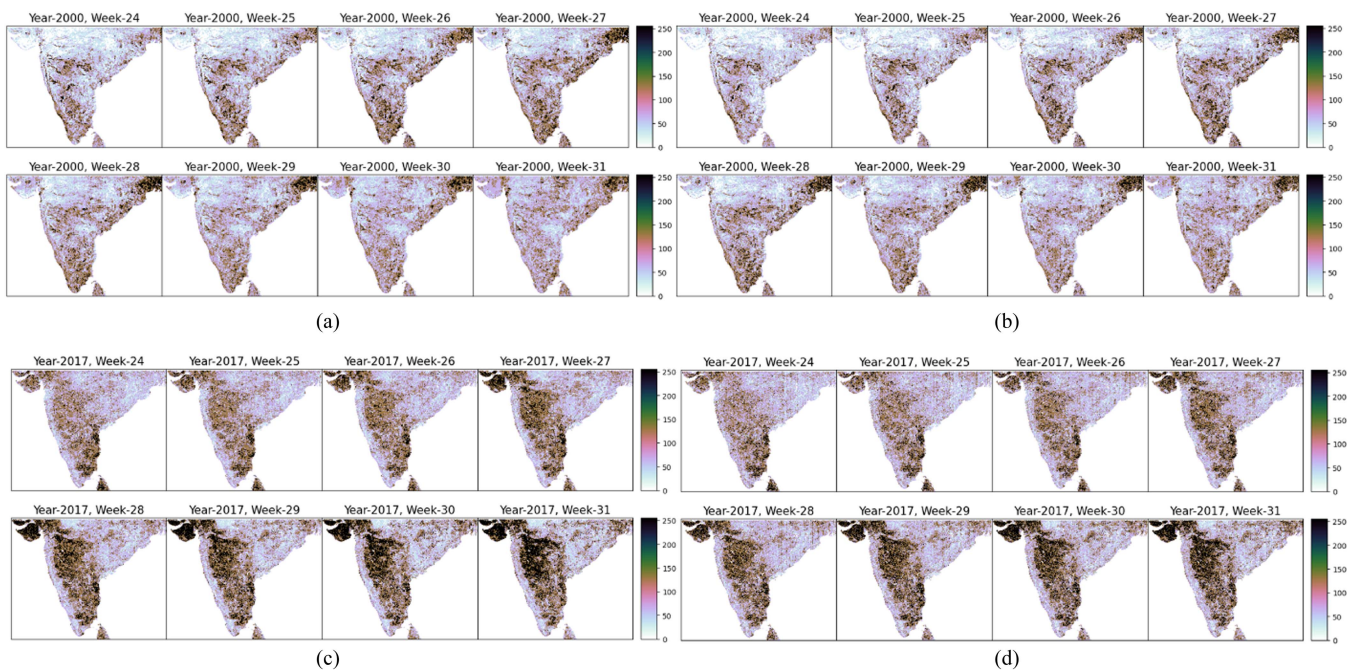

Fig. 11. Comparison of drought-hit peninsular India for the year 2000 through (a) P2P and (b) BiCP2P and nondrought-hit peninsular India for the year 2017 through the models (c) P2P and (d) BiCP2P.

consequences appropriately. The key advantages of choosing generative models for the regression task in the present research are exceptional prediction metrics and realistic and finer prediction outputs. Additionally, the proposed frameworks also share the benefits of projecting the same models for both regression and further classification into various attributes (of land types), as well as the generation of new data samples embodied similar to the training set to aid in the analysis of potential land scenarios in the near future at relatively nominal computational cost. Additionally, the obtained results can further be extended to perform seasonal trend analysis by observing the seasonal drought maps that capably explain the present scenario and assist in short-term drought forecasting.

Conclusively, several momentous advantages inferred in this work encompass the quintessential performance of the proposed models, P2P and BiCP2P, across all the datasets, which are diverse in magnitude, terrain, and topology, with the incurred drought maps by suggested models complying with the ground truth image. Moreover, the suggested models are able to demonstrate the drought and nondrought segmentation adequately, as witnessed for the years 2000 and 2017, respectively. The P2P and BiCP2P models can be further customized for an assortment of applications, such as precipitation forecasting and crop yield analysis, among others, unlike other ML/DL-models, which are highly complex for regeneration for different applications, such as models like ConvLSTM and LSTM. Furthermore, statistical models, such as the Mann-Kendall test, are parameter-specific and are not adaptable for multiple applications. The generative models, P2P and BiCP2P, can be trained additionally on several more related features to predict and generate more accurate future VHI samples, which can aid in disaster mitigation. The computational time and resources consumed by the models are nominal as compared to other ML/DL models, giving it an edge over the others. Furthermore, the models can be trained to generate seasonal and condition-specific outcomes by supplying suitable data, such as by providing seasonal information, the future seasonal scenario of the ROI can be predicted, and also, the inclining or declining trend of greenery can be traced. However, the P2P and BiCP2P models cannot demarcate between the seasonal/geographical conditions unless specified manually. Due to the widescale topological variations within the ROI, the climatic, regional, and natural interferences are not explicitly taken into account in this study and can be recognized as one of the future scopes for the current work. Alternatively, the VHI dataset is delivered to the models with the uniform data assumption. The models can provide forecasts dependent on the input datasets, and the forecast precision also relies in some ways on the data quality supplied to it. Hence, the data quality should be monitored before supplying it to the models. Besides, natural variables impacting the vegetative capacity of the land, such as high winds, acid rain, or pest-infested crops, are exceptions that must be manually differentiated and cannot be distinctly detected through the existing model alignment. Such natural factors are uncommon and intend to be demarcated as an outlier during the data preprocessing step. Moreover, the dataset employed in this study features a weekly temporal scale, enabling it to present short-term scenarios of the ROI and significantly influence the continual surveillance of crops and land cover. Nevertheless, the data's temporality scale may be altered and delivered to the generative models, which possess the competence to yield precise results at various envisioned timelines, both short- and long-term. Remarkably, alternative statistical or AI-based models seldom exhibit the versatility that the P2P and BiCP2P models practice, producing precise results at various temporalities.

VI. CONCLUSION

The current article delivers the novel application of two DL-oriented models—P2P and a novel integrated BiCP2P model, for vegetative drought analysis utilizing satellite data. The proposed models are implemented on four datasets from 1981 to 2022 and are compared with several state-of-the-art ML/DL-based models. Furthermore, the performance metrics gained by the P2P and BiCP2P models are superior to the reference models with mean R2, MSE, and MAE for dataset - I conforming to 0.971, 0.0016, and 0.020 (P2P) and 0.963, 0.0021, and 0.0239 (BiCP2P), for dataset - II achieving values of 0.95, 0.0018, and 0.023 (P2P) and 0.9462, 0.0021, and 0.0254 (BiCP2P), for dataset - III acquiring values of 0.92, 0.0018, and 0.0235 (P2P) and 0.92, 0.0021, and 0.024 (BiCP2P) and finally for dataset - IV gaining up to 0.93, 0.0033, and 0.032 (P2P) and 0.94, 0.0042, and 0.033 (BiCP2P), respectively. The models worked productively across diverse ROIs involving different topological and geophysical alignments. Furthermore, the novel amalgamation of rainfall and VHI characteristics performs efficiently for VHI-based drought prediction. Additionally, the recommended models exhibited precise segregation of drought and nondrought sectors, guaranteeing the high metric scores attained and the potential of the models in short-term drought forecasting with multiple databases and adaptability to other applications. The future scope of this study entails performing seasonal trend analysis incorporating seasonal drought maps or observing drought probability with various natural constraints (e.g., pests, temperature) on the green cover of the ROI under consideration. Moreover, the analysis can be strengthened by diversifying the feature sets through a larger ROI or boosting the temporality scale.

REFERENCES

[1] P. Venkateswrlu, "Remote sensing and GIS to combat drought disaster: An Indian example," in *Proc. IEEE Int. Geosci. Remote Sens. Symp.*, vol. 4, 2004, pp. 2294–2297.

[2] Z. Zhang, W. Xu, Z. Shi, and Q. Qin, "Establishment of a comprehensive drought monitoring index based on multisource remote sensing data and agricultural drought monitoring," *IEEE J. Sel. Topics Appl. Earth Observ. Remote Sens.*, vol. 14, pp. 2113–2126, Jan. 2021.

[3] S. Y. J. Prasetyo, K. D. Hartomo, M. C. Paseleng, D. W. Candra, and B. H. Simanjuntak, "The machine learning to detect drought risk in Central Java using Landsat 8 OLI remote sensing images," in *Proc. IEEE 5th Int. Conf. Sci. Technol.*, 2019, vol. 1, pp. 1–6.

[4] M. Jalili, J. Gharibshah, S. M. Ghavami, M. Beheshtifar, and R. Farshi, "Nationwide prediction of drought conditions in Iran based on remote sensing data," *IEEE Trans. Comput.*, vol. 63, no. 1, pp. 90–101, Jan. 2014.

[5] S. Kumar, S. A. Ahmed, and J. Karkala, "Intensity and spatiotemporal variations of drought in Tumakuru district, India using drought indices," *Geocarto Int.*, vol. 37, no. 27, pp. 17642–17658, Oct. 2022.

[6] H. Heydari, M. V. Zoej, Y. Maghsoudi, and S. Dehnavi, "An investigation of drought prediction using various remote-sensing vegetation indices for different time spans," *Int. J. Remote Sens.*, vol. 39, no. 6, pp. 1871–1889, Jan. 2018.

[7] D. L. Miller et al., "Seasonal and interannual drought responses of vegetation in a California urbanized area measured using complementary remote sensing indices," *ISPRS J. Photogram. Remote Sens.*, vol. 183, pp. 178–195, Jan. 2022.

[8] F. Zambrano, A. Vrieling, A. Nelson, M. Meroni, and T. Tadesse, "Prediction of drought-induced reduction of agricultural productivity in Chile from MODIS, rainfall estimates, and climate oscillation indices," *Remote Sens. Environ.*, vol. 219, pp. 15–30, Dec. 2018.

[9] Z. Li, Y. Han, and T. Hao, "Assessing the consistency of remotely sensed multiple drought indices for monitoring drought phenomena in continental China," *IEEE Trans. Geosci. Remote Sens.*, vol. 58, no. 8, pp. 5490–5502, Aug. 2020.

[10] Z. Xu et al., "Trends in global vegetative drought from long-term satellite remote sensing data," *IEEE J. Sel. Topics Appl. Earth Observ. Remote Sens.*, vol. 13, pp. 815–826, Feb. 2020.

[11] J. Lu, L. Jia, C. Zheng, J. Zhou, M. V. Hoek, and K. Wang, "Characteristics and trends of meteorological drought over China from remote sensing precipitation datasets," in *Proc. IEEE Int. Geosci. Remote Sens. Symp.*, 2016, pp. 7581–7584.

[12] S. Yang, C. Liu, and R. Sun, "The temporal and spatial analysis of drought in Yellow River Basin using remote sensing and GIS," in *Proc. IEEE Int. Geosci. Remote Sens. Symp.*, 2003, vol. 4, pp. 2290–2292.

[13] A. Shahabfar, A. Ghulam, and C. Conrad, "Understanding hydrological repartitioning and shifts in drought regimes in Central and South-West Asia using MODIS derived perpendicular drought index and TRMM data," *IEEE J. Sel. Topics Appl. Earth Observ. Remote Sens.*, vol. 7, no. 3, pp. 983–993, Mar. 2014.

[14] G. Berhan, S. Hill, T. Tadesse, and S. Atnafu, "Drought prediction system for improved climate change mitigation," *IEEE Trans. Geosci. Remote Sens.*, vol. 52, no. 7, pp. 4032–4037, Jul. 2014.

[15] G. B. Demisse, T. Tadesse, Y. Bayissa, S. Atnafu, M. Argaw, and D. Nedaw, "Vegetation condition prediction for drought monitoring in pastoralist areas: A case study in Ethiopia," *Int. J. Remote Sens.*, vol. 39, no. 14, pp. 4599–4615, Jan. 2018.

[16] J. S. Shukla and R. J. Pandya, "ML-based vegetative drought prediction employing satellite remote sensing and precipitation datasets," in *Proc. IEEE 13th Int. Conf. Pattern Recognit. Sys.*, 2023, pp. 1–7.

[17] S. Chaudhari, V. Sardar, D. Rahul, M. Chandan, M. S. Shivakale, and K. Harini, "Performance analysis of CNN, AlexNet and VGGNet models for drought prediction using satellite images," in *Proc. Asian Conf. Innov. Technol.*, 2021, pp. 1–6.

[18] G. Ghazaryan, S. Skakun, S. König, E. E. Rezaei, S. Siebert, and O. Dubovyk, "Crop yield estimation using multi-source satellite image series and deep learning," in *Proc. IEEE Int. Geosci. Remote Sens. Symp.*, 2020, pp. 5163–5166.

[19] W. S. Hu, H. C. Li, L. Pan, W. Li, R. Tao, and Q. Du, "Spatial–Spectral feature extraction via deep ConvLSTM neural networks for hyperspectral image classification," *IEEE Trans. Geosci. Remote Sens.*, vol. 58, no. 6, pp. 4237–4250, Jun. 2020.

[20] C. Liu, H. Li, A. Su, S. Chen, and W. Li, "Identification and grading of maize drought on RGB images of UAV based on improved U-Net," *IEEE Geosci. Remote Sens. Lett.*, vol. 18, no. 2, pp. 198–202, Feb. 2021.

[21] S. Zhong, Z. Xu, and L. Cao, "Evaluating performance of prediction of vegetative drought using classic and recent sequence-based models," in *Proc. IEEE 9th Int. Conf. Agro-Geoinformatics*, 2021, pp. 1–6.

[22] W. Tian, J. Wu, H. Cui, and T. Hu, "Drought prediction based on feature-based transfer learning and time series imaging," *IEEE Access*, vol. 9, pp. 101454–101468, Jul. 2021.

[23] D. Yang, S. Zhong, X. Mei, X. Ye, F. Niu, and W. Zhong, "A comparative study of several popular models for near-land surface air temperature estimation," *Remote Sens.*, vol. 15, no. 4, pp. 1–21, Feb. 2023.

[24] G. Hinge, J. Piplodiya, A. Sharma, M. A. Hamouda, and M. M. Mohamed, "Evaluation of hybrid wavelet models for regional drought forecasting," *Remote Sens.*, vol. 14, no. 24, pp. 1–17, Dec. 2022.

[25] I. Okwuchi, L. Nassar, F. Karray, and K. Ponnambalam, "Deep learning ensemble based model for time series forecasting across multiple applications," in *Proc. IEEE Int. Conf. Syst. Man Cybern.*, 2020, pp. 3077–3083.

[26] S. Park, J. Im, D. Han, and J. Rhee, "Short-term forecasting of satellite-based drought indices using their temporal patterns and numerical model output," *Remote Sens.*, vol. 12, no. 21, pp. 2072–4292, Oct. 2020.

[27] A. P. Kogekar, R. Nayak, and U. C. Pati, "A CNN-BiLSTM-SVR based deep hybrid model for water quality forecasting of the river Ganga," in *Proc. IEEE 18th India Council Int. Conf.*, 2021, pp. 1–6.

[28] R. Azad, M. A. Aghbolaghi, M. Fathy, and S. Escalera, "Bi-directional ConvLSTM U-net with densely connected convolutions," in *IEEE/CVF Int. Conf. Comp. Vis. Workshop*, 2019, pp. 406–415.

[29] L. Lin, J. Wu, P. Cheng, K. Wang, and X. Tang, "BLU-GAN: Bi-directional ConvLSTM U-Net with generative adversarial training for retinal vessel segmentation," in *Intelligent Computing and Block Chain*, vol. 1385. Berlin, Germany: Springer, Mar. 2021, pp. 3–13.

[30] F. Zhu, F. Ye, Y. Fu, Q. Liu, and B. Shen, "Electrocardiogram generation with a bidirectional LSTM-CNN generative adversarial network," *Sci. Rep.*, vol. 9, no. 1, pp. 2045–2322, May 2019.

[31] I. Goodfellow et al., "Generative adversarial networks," *Commun. ACM*, vol. 63, no. 11, pp. 139–144, Oct. 2020.

[32] H. Zhang, Y. Song, C. Han, and L. Zhang, "Remote sensing image spatiotemporal fusion using a generative adversarial network," *IEEE Trans. Geosci. Remote Sens.*, vol. 59, no. 5, pp. 4273–4286, May 2021.

[33] N. Gao et al., "Generative adversarial networks for spatio-temporal data: A survey," *ACM Trans. Intell. Syst. Technol.*, vol. 13, no. 2, pp. 1–25, Apr. 2022.

[34] P. Jian, K. Chen, and W. Cheng, "GAN-based one-class classification for remote-sensing image change detection," *IEEE Geosci. Remote Sens. Lett.*, vol. 19, pp. 1–5, Apr. 2022.

[35] M. Mirza and S. Osindero, "Conditional generative adversarial nets," *ArXiv*, vol. abs/1411.1784, Nov. 2014.

[36] P. Isola, J. Y. Zhu, T. Zhou, and A. A. Efros, "Image-to-image translation with conditional adversarial networks," in *Proc. IEEE Conf. Comp. Vis. Pattern Recognit.*, 2017, pp. 5967–5976.

[37] S. Sun, L. Mu, R. Feng, L. Wang, and J. He, "GAN-based LUCC prediction via the combination of prior city planning information and land-use probability," *IEEE J. Sel. Topics Appl. Earth Observ. Remote Sens.*, vol. 14, pp. 10189–10198, Aug. 2021.

[38] J. S. Shukla and R. J. Pandya, "Predictive modeling of vegetative drought using ML/DL approach on temporal satellite data," in *Proc. IEEE Int. Conf. Ind. Artif. Intell. Commun. Technol.*, 2023, pp. 277–283.

[39] R. Sedona, C. Paris, G. Cavallaro, L. Bruzzone, and M. Riedel, "A high-performance multispectral adaptation GAN for harmonizing dense time series of Landsat-8 and Sentinel-2 images," *IEEE J. Sel. Topics Appl. Earth Observ. Remote Sens.*, vol. 14, pp. 10134–10146, Sep. 2021.

[40] H. Vathsala and S. G. Koolagudi, "Prediction model for peninsular Indian summer monsoon rainfall using data mining and statistical approaches," *Comput. Geosci.*, vol. 98, pp. 55–63, Jan. 2017.

[41] K. Agarwal and S. Vadhera, "Short-term wind speed forecasting of coastal line of peninsular India using NARX models," in *Proc. 2nd Int. Conf. Intell. Tech.*, 2022, pp. 1–6.

[42] S. Zhong, L. Di, Z. Sun, Z. Xu, and L. Guo, "Investigating the long-term spatial and temporal characteristics of vegetative drought in the contiguous United States," *IEEE J. Sel. Topics Appl. Earth Observ. Remote Sens.*, vol. 12, no. 3, pp. 836–848, Mar. 2019.

[43] D. Pai, M. Rajeevan, O. Sreejith, B. Mukhopadhyay, and N. Satbha, "Development of a new high spatial resolution ($0.25° \times 0.25°$) long period (1901-2010) daily gridded rainfall data set over India and its comparison with existing data sets over the region," *MAUSAM*, vol. 65, no. 1, pp. 1–18, Jan. 2014.

[44] Y. Kang, S. Gao, and R. E. Roth, "Transferring multiscale map styles using generative adversarial networks," *Int. J. Cartogr.*, vol. 5, no. 2/3, pp. 115–141, May 2019.

[45] D. Iskandaryan, F. Ramos, and S. Trilles, "Bidirectional convolutional LSTM for the prediction of nitrogen dioxide in the city of Madrid," *PLoS ONE*, vol. 17, no. 6, pp. 1–20, Jun. 2022.

[46] X. Shi, Z. Chen, H. Wang, D. Y. Yeung, W. K. Wong, and W. C. Woo, "Convolutional LSTM network: A machine learning approach for precipitation nowcasting," in *Proc. 28th Int. Conf. Neur. Info. Proc. Syst.*, 2015, vol. 1, pp. 802–810.

[47] J. Sun, Y. Jiang, and J. Lin, "Convolutional LSTM network for forecasting correlations between stocks based on spatiotemporal sequence," in *Proc. IEEE 19th Int. Conf. Ind. Inform.*, 2021, pp. 1–6.

[48] X. Zhang, R. Obringer, C. Wei, N. Chen, and D. Niyogi, "Droughts in India from 1981 to 2013 and implications to wheat production," *Sci. Rep.*, vol. 7, no. 1, pp. 2045–2322, Mar. 2017.

Jyoti S. Shukla received the B.E. degree in electronics and communication from Gujarat Technological University, Ahmedabad, India, in 2019. She is currently working toward the M.S. by Research degree in AI/ML and image processing with the Electrical, Electronics, and Communications Engineering Department, Indian Institute of Technology (IIT) Dharwad, Dharwad, India.

She is currently working as a Researcher with TCS Research, India. Her research interests include understanding and developing artificial intelligence-based tools for computer vision and remote sensing applications, and satellite image processing.

Rahul Jashvantbhai Pandya (Senior Member, IEEE) received the M.Tech. degree in optoelectronics and optical communication from the Electrical Engineering Department, Indian Institute of Technology, Delhi, India, in 2010, and the Ph.D. degree in optical networks from the Bharti School of Telecommunication, Indian Institute of Technology, in 2014.

He worked as the Senior Network Design Engineer in the Optical Networking Industry at Infinera Pvt. Ltd., Bangalore, India, from 2014 to 2018. Later, from 2018 to 2020, he worked as an Assistant Professor at the ECE Department, National Institute of Technology, Warangal, India. Currently, he is with the Electrical, Electronics, and Communication Engineering (EECE) Department, Indian Institute of Technology, Dharwad, India. He is working on multiple projects, such as SERB, SPARC, SGNF, and RSM. His research interests include wireless communication, optical communication, optical networks, computer networks, machine learning, and artificial intelligence.